Confinement and Transport in the National Spherical Torus Experiment (NSTX)

S. M. Kaye[1], F.M. Levinton[2], D. Stutman[3], K. Tritz[3], H. Yuh[2], M.G. Bell[1], R.E. Bell[1], W. Horton[4], J. Kim[4], B.P. LeBlanc[1], R. Maingi[5], E. Mazzucato[1], J.E. Menard[1], D. Mikkelsen[1], H. Park[1], G. Rewoldt[1], S.A. Sabbagh[6], D.R. Smith[1], W. Wang[1] and the NSTX Group

email: skaye@pppl.gov

[1] *Princeton Plasma Physics Laboratory, Princeton University, Princeton, NJ 08543*
[2] *Nova Photonics Inc., Princeton, NJ 08540*
[3] *The Johns Hopkins University, Baltimore MD 21218*
[4] *Institute For Fusion Studies, University of Texas, Austin, TX 78712*
[5] *Oak Ridge National Laboratory, Oak Ridge, TN 37831*
[6] *Dept. of Applied Physics, Columbia University, NYC, NY 10027*

Abstract

NSTX operates at low aspect ratio (R/a≤1.3) and high beta (up to 40%), allowing tests of global confinement and local transport properties that have been established from higher aspect ratio devices. NSTX plasmas are heated by up to 7 MW of deuterium neutral beams with preferential electron heating as expected for ITER. Confinement scaling studies indicate a strong B_T dependence, with a current dependence that is weaker than that observed at higher aspect ratio. Dimensionless scaling experiments indicate a strong increase of confinement with decreasing collisionality and a weak degradation with beta. The increase of confinement with B_T is due to reduced transport in the electron channel, while the improvement with plasma current is due to reduced transport in the ion channel related to the decrease in neoclassical transport levels. Improved electron confinement has been observed in plasmas with strong reversed magnetic shear, showing the existence of an electron internal transport barrier (eITB). Perturbative studies show that while L-mode plasmas with reversed magnetic shear and an eITB exhibit slow changes of L_{Te} across the profile after the pellet injection, H-mode plasmas with a monotonic q-profile and no eITB show no change in this parameter after pellet injection, indicating the existence of a critical gradient that may be related to the q-profile. Both linear and non-linear simulations indicate the potential importance of ETG modes at the lowest B_T. Localized measurements of high-k fluctuations exhibit a sharp decrease in turbulence levels across the L-H transition, associated with a decrease in calculated linear growth rates across a wide k-range, from the ITG/TEM regime up to the ETG regime.

1. Introduction

The National Spherical Torus Experiment (NSTX) provides a unique view into plasma transport and turbulence properties by operating at high toroidicity/low aspect ratio (R/a~1.3), high β_T (up to 40%), and low collisionality [1,2]. This is accomplished with up to 7 MW of ~90 keV deuterium neutral beam injection power into deuterium plasmas in either the lower single null or double null configuration. NSTX operates at low toroidal field (B_T=0.35 to 0.55 T) and relatively high plasma current (I_p up to 1.5 MA). The neutral beams heat the electrons preferentially, as is expected for α-heating in ITER. The large range of accessible β_T allows exploration of turbulence spanning both electrostatic and electromagnetic regimes. The low toroidal field and large neutral beam induced rotation give rise to high levels of rotational shear that can influence transport. Finally, the low toroidal field results in a relatively large electron gyroradius (ρ_e~0.1 mm), which allows electron scale turbulence to be measured locally. Thus, NSTX can address fundamental transport and turbulence issues that are critical to both basic toroidal confinement and future devices.

The purpose of this study is to address both the global confinement and local transport properties of NSTX plasmas. This will be studied through results of dedicated scans primarily

in H-mode plasmas, coupled with turbulence measurements and both linear and non-linear turbulence simulations. Within the past two years, NSTX has implemented two key diagnostics; the first being a tangential scattering system capable of measuring turbulence locally over a k_r from 2 to 24 cm^{-1}, which covers the upper end of the ITG/TEM up through the ETG mode range [3]. Second, a 12-point Motional Stark Effect diagnostic, which measures the magnetic field pitch, allows the local transport properties to be related to details of the q-profile. In the following sections we will present results from the global confinement scaling studies, followed by inferences of the local transport for both the ions and the electrons. The confinement and transport studies will then be tied into both measurements of high-k turbulence and results of linear and non-linear turbulence/transport calculations to understand the root cause of the transport in NSTX. It is found that while the ion transport is near neoclassical levels, the electron transport is anomalous. ETG modes appear to be a potential candidate for the electron transport under certain conditions.

2. Confinement Scaling

Previous statistical studies of energy confinement in H-mode plasmas on NSTX indicated a stronger dependence on toroidal magnetic field ($\tau_E \sim B_T^{1.0}$) and a weaker dependence on plasma current ($\tau_E \sim I_p^{0.6}$) than at conventional aspect ratio [4]. The confinement scalings derived therein transformed into a dimensionless scaling that exhibited no degradation of $B\tau_E$ with β_T, important to the success of the ITER advanced operating regime. It was also found that the ITER98PB(y,2) [5] scaling did not adequately describe the NSTX confinement times, and the NSTX dataset submitted to the ITPA H-mode database, along with data from the low aspect ratio MAST and START devices and the standard selection set of higher aspect ratio data [6], were used to develop new scalings [7]. This last study focused on the ε (=a/R) and β_T dependences, parameters for which the set of low aspect ratio data have high leverage. The new scalings showed a stronger scaling with inverse aspect ratio ($\tau_E \sim \varepsilon^{1.03}$ vs $\varepsilon^{0.58}$ as in 98y,2) and a weaker degradation with β_T ($B\tau_E \sim \beta_T^{-0.5}$ vs $\beta_T^{-0.9}$ as in 98y,2). The change in the ε coefficient was accompanied by changes in the I_p, B_T and R coefficients as well.

One of the issues in the NSTX dataset used for the above studies was a correlation among various engineering variables, most notably between line-averaged density and either plasma current or heating power. Consequently, dedicated scans were recently undertaken in an attempt to break this correlation and determine the parametric dependence on both B_T and I_p to a greater degree of certainty. For these scans, barely lower single null discharges with elongations of 2.1 and triangularities of 0.6 were run at constant injected beam power of 4 MW. Scans of toroidal field (0.35 to 0.55 T) were performed at fixed I_p of 0.7 and 0.9 MA, and an I_p scan was performed at B_T=0.55 T. Scans at lower toroidal field or higher current resulted in discharges with large low-n activity due to q-limits. The plasma densities in the discharges were comparable, allowing direct comparison and determination of the individual scalings. A B_T/I_p scan was also performed at fixed q, as were individual scans of the dimensionless parameters β_T and ν_e (electron collisionality) while attempting to hold other dimensionless variables, including ρ_e, toroidal velocity shear and q constant.

An overview of the B_T scan at I_p=0.7 MA is shown in Fig. 1, where plasma current, density, D_α and total stored energy as calculated by the LRDFIT equilibrium reconstruction code are plotted from the top for discharges at 0.35, 0.45 and 0.55 T respectively. The plasma density for all three toroidal fields track each other well, allowing a direct comparison among the discharges at constant beam power, density and plasma current. The normalized beta values for these discharges reach a maximum of 5.4, which is just below the ideal wall stability limit

[8]. The total fast ion losses due to classical processes (shine-through, bad orbits and charge-exchange) vary from 13 to 20% for the three toroidal fields. As seen in the bottom panel, the total stored energy increases with increasing B_T.

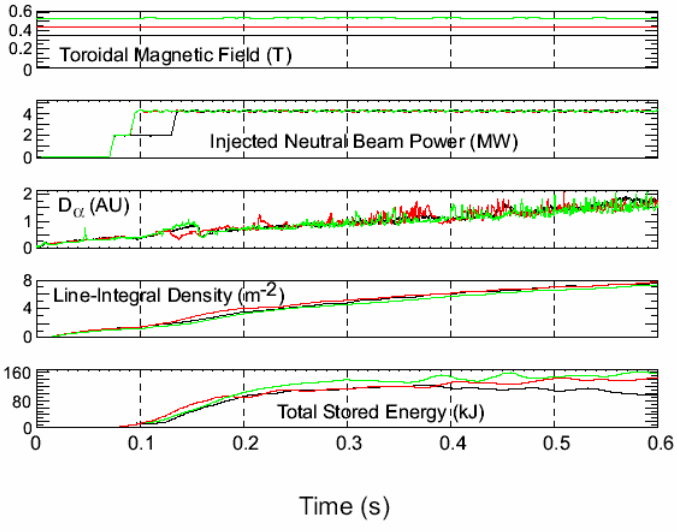

Fig. 1 Time evolution of discharge characteristics for the B_T scan at I_p=0.7 MA.

The scaling of both the thermal and global confinement time as a function of toroidal field is shown in Fig. 2. Here the thermal and global confinement times are defined as $\tau_{E,th}=W_{th}/P_L$ where $P_L=P_{NBI}+P_{OH}-P_{loss}-dW/dt$, P_{loss} includes shine-thru, bad-orbit and charge-exchange losses, and $\tau_{E,G}=(W_{th}+W_{fast})/P_L$, with W_{th} being the stored energy in the thermal plasma and W_{fast} the stored energy in the fast ion population. The confinement times clearly show a strong dependence on toroidal field, with $\tau_{E,th} \sim B_T^{0.91}$ and $\tau_{E,G} \sim B_T^{0.81}$, which is a stronger dependence than observed at higher aspect ratio. A similar toroidal field scan was performed at 0.9 MA, although the lowest toroidal field accessed was 0.4 T. to avoid low-n MHD activity. For the 0.9 MA scan, both the thermal and global confinement times scaled as $B_T^{0.6}$, slightly weaker than at the lower current.

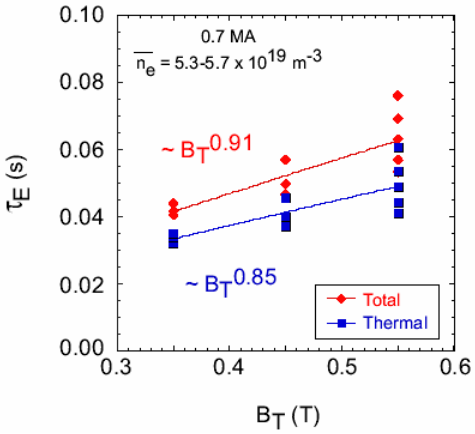

Fig. 2 Scaling of global and thermal energy confinement times for B_T scan at I_p=0.7 MA

The dependence of confinement on plasma current is weaker. This is seen in Fig. 3, where the results of a current scan from 0.7 to 1.1 MA at 0.55 T are shown. Both the thermal and global confinement times scale as $I_p^{0.4}$ at constant toroidal field. Scans were also performed at fixed q (fixed I_p/B_T), and the discharges in these dedicated scans indicated an $I_p^{1.3-1.5}$ (or equivalently $B_T^{1.3-1.5}$) dependence, stronger than the $I_p^{1.1}$ (or $B_T^{1.1}$) dependence at fixed q in the ITER98PB(y,2 scaling.

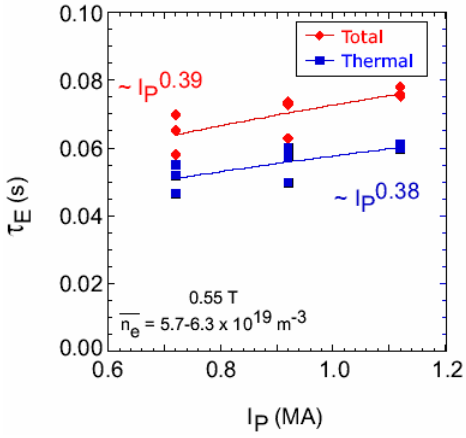

Fig. 3 Scaling of global and thermal energy confinement times for I_p scan at B_T=0.55T

Dimensionless parameter scans to investigate the dependence of confinement on both ν_e^* and β_T were performed at constant q. The dependence of collisionality was obtained by varying both toroidal field and plasma density. The results are shown in Fig. 4a. The top part of the figure shows β_T and ρ_e as ν_e^* was varied, and while there was a factor of three variation in ν_e^*, there was only a 20% variation in these other parameters. The variation of $B\tau_E$ with ν_e is

strong, going as approximately ν_e^{*-1} (confinement improving as the discharge gets deeper into the trapped electron regime). This is in contrast to the $\nu_e^{*-0.4}$ dependence seen at higher aspect

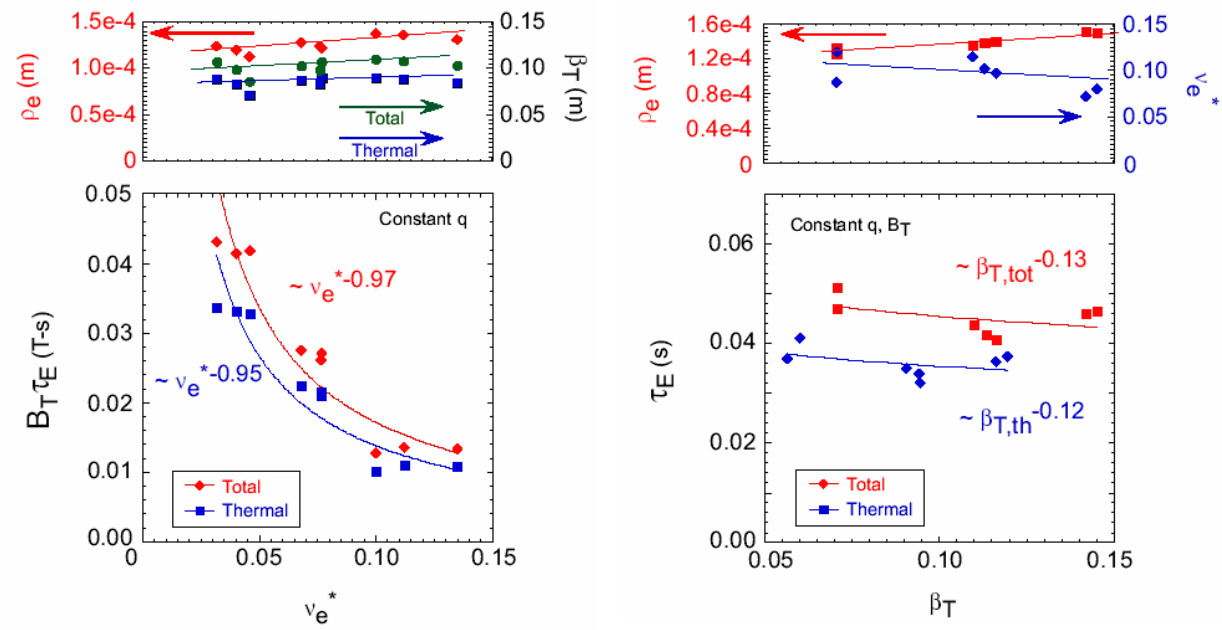

Fig. 4a Confinement scaling results from collisionality scan (left) and b) beta scan (right). The β_T scan was performed at constant B_T.

ratio [6]. The result for the β_T scaling is shown in Fig. 4b. Here, the β_T variation was accomplished by varying density and input power at constant toroidal field (and constant q). ν_e^* and ρ_e varied only 20% over the range of the β_T variation, which was a factor of 2.5. The confinement times degrade only weakly with β_T, going as $\beta_T^{-0.10}$. These results are consistent with the weak β_T scaling observed in dedicated JET and DIII-D scans [9,10]

3. Local Transport Results

The electron and ion temperature profiles for the three toroidal fields in the 0.7 MA, B_T scan are shown in Fig. 5a and b. The colored band for each toroidal field represents the envelope of profiles measured for that condition (i.e., several discharges at each condition were produced to study reproducibility). It is clearly seen that as the toroidal field increases the electron temperature profile broadens considerably, while the central temperature remains approximately constant. This behavior is very different from what was observed at higher aspect ratio, where it was the central T_e that was most affected by variations in the toroidal field [11]. The ion temperature profiles, on the other hand, show less variation with B_T. For all

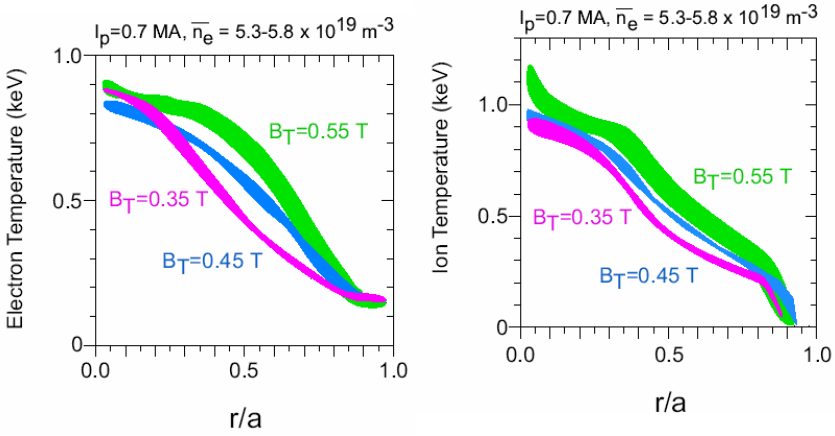

Fig. 5a Electron (left) and b) ion temperature profiles from the B_T scan at I_p=0.7 MA. The band for each condition is the envelope of profiles for that condition.

the discharges in this scan, the density profiles essentially overlaid each other.

Transport analysis of these discharges was done using the TRANSP analysis code, which folds in measured temperature and density (including impurity) profiles, rotation velocity, radiated power, and it computes the beam ion deposition and density using a Monte-Carlo approach to determine the sources and losses of energy and particles. From these terms, the local particle and thermal diffusivities are calculated. The electron thermal and ion thermal diffusivities for the discharges in the B_T scan are shown in Fig. 6a and b. Apparent in Fig. 6 is that it is the electron thermal diffusivity that varies the most as the toroidal field is varied. As can be seen in Fig. 6a, the χ_e decreases significantly outside of r/a=0.5 as the toroidal field increases, consistent with the broadening of the electron temperature profile with increasing toroidal field. The χ_e profiles exhibit a pivot point around r/a=0.5; inside of this radius the χ_e increases with increasing toroidal field, which is due primarily to an increased flattening of the T_e profile in this region with higher B_T. The higher χ_e in this low volume core region does not affect the electron or thermal confinement increase with B_T, which apparently is controlled more by the transport outside r/a=0.5. The ion thermal diffusivity changes very little with B_T, as can be seen in Fig. 6b, and the χ_i values are close to the neoclassical transport level as determined by the NCLASS formulation [12]. Beyond r/a=0.5, $\chi_i > \chi_e$ at the higher B_T.

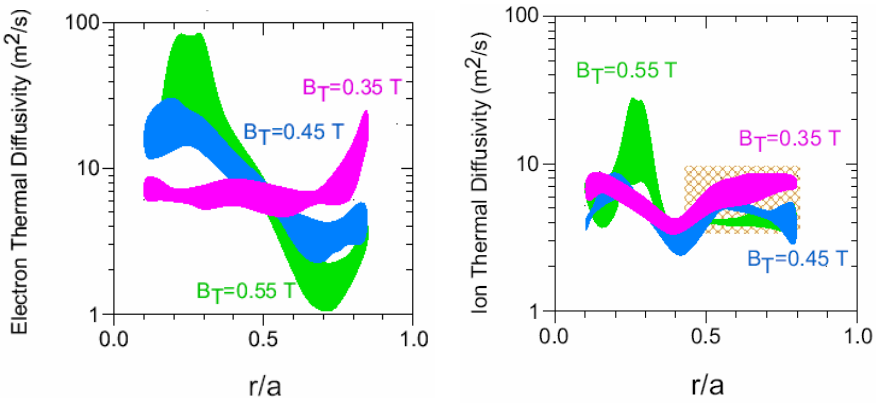

Fig. 6a Electron (left) and b) ion thermal diffusivities from the B_T scan at I_p=0.7 MA. The hatched region in b) represents the range of neoclassical ion transport as calculated by NCLASS.

In contrast to the B_T scaling results, it is more the ions than the electrons that control the variation of confinement in the I_p scan. In Fig. 7a and 7b are plotted the electron and ion thermal diffusivities for the three different currents in the I_p scan at B_T= 0.55 T. As can be seen in Fig. 7a, the χ_e changes only slightly as the plasma current is increased, while, in Fig. 7b, the χ_i decreases with increasing current outside of r/a=0.4, but change very little inside that radius. As was the case for the B_T scan, the ion transport is near the neoclassical level. The neoclassical level here is determined by GTC-NEO [13], which takes into

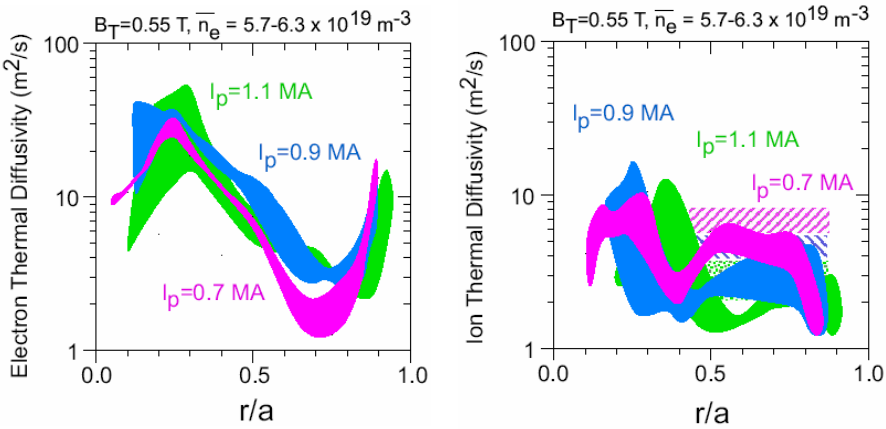

Fig. 7a Electron (left) and b) ion thermal diffusivities for the I_p scan at 0.55T. The hatched region in b) represents ranges of neoclassical ion transport calculated by GTC-NEO for each condition.

account non-local (e.g. finite banana width) effects, and χ_i varies with I_p as does $\chi_{i,nc}$.

In addition to the dependences of the inferred transport coefficients on the global discharge parameters, the local transport characteristics are found to be dependent also on local parameters such as the magnetic shear. A set of experiments in low density L-mode plasmas was carried out to study this effect utilizing the 12 point MSE diagnostic for an accurate reconstruction of the current profile. The experiments showed a peaking of the plasma temperature profiles (**I**nternal **T**ransport **B**arriers) in the reversed magnetic shear plasmas as compared to plasmas with monotonic q-profiles. The peaking, and a reduction in transport in both the ions and electrons, was found to be predominantly in the reversed shear region. Perturbative studies using Li pellets showed that while L-mode plasmas with reversed magnetic shear and an electron ITB exhibited slow changes of L_{Te} after the pellet injection, H-mode plasmas with a monotonic q-profile show no change in this parameter after pellet injection, indicating stiff profiles and the possible existence of a critical gradient [14].

4. Turbulence Measurements and Simulations

Turbulence measurements and gyrokinetic calculations have helped identify the possible sources of transport in NSTX plasmas. Fig. 8 shows a time history of fluctuation levels for k_r=4 to 24 cm^{-1} as measured by the tangential scattering system for a 2 MW discharge. The measurements were localized to a radius from r/a=0.7 to 0.8 during the course of the discharge. The actual relative fluctuation level is obtained by scaling the level plotted by the "x" factor shown in each panel (i.e., the fluctuation level for 4 cm^{-1} is 80x that for 24 cm^{-1}). What is clear in the figure is that the fluctuation levels decrease for all k_r going from the L- to the H-mode at 0.2 s, and they increase as the discharge transitions back into the L-mode at ~0.5 s. The spikes seen in the 24 cm^{-1} channel are coherent electrostatic bursts that are associated with ELMs. Associated with the decrease in fluctuation level during the H-mode is a reduction in both the electron and ion thermal diffusivities going from L to H. The electron transport is anomalous for both phases, but the ion transport is reduced from approximately 5 to 10 times, to within a factor of two of the neoclassical level. $\chi_e > \chi_i$ during both the L- and H-phases for this discharge.

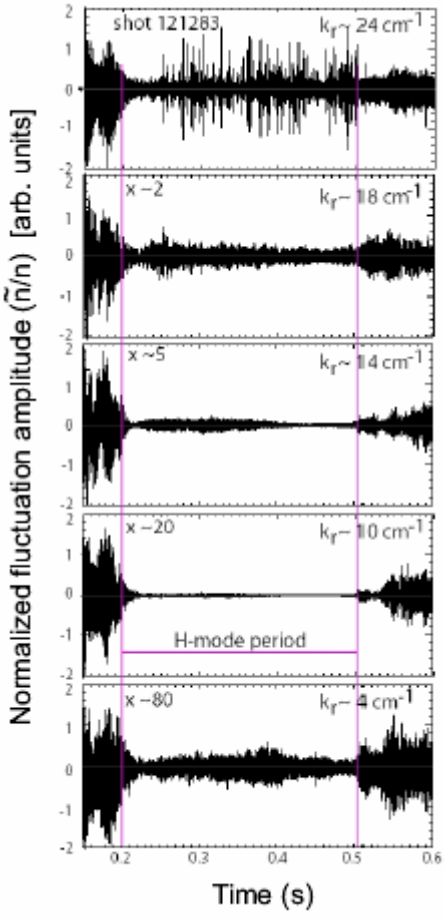

Fig. 8 Time evolution of density fluctuation levels normalized to local density at r/a=0.7-0.8. The H-mode lasts from 0.2 , to 0.51 s.

Linear GS2 [15] calculations have been performed to try to identify the source of the turbulence and its reduction. The linear growth rates and ExB shearing rates for the early L-phase and the H- phase calculated at the turbulence measurement location are plotted in Fig. 9 as a function of $k_\theta \rho_s$. Both the ITG/TEM and ETG modes are linearly unstable during the L-phase, and their growth rates exceed the ExB shearing rate by at least a factor of several for the entire wavenumber range. As the discharge transitions into the H-phase, and the calculated electron and ion transport decrease, the linear

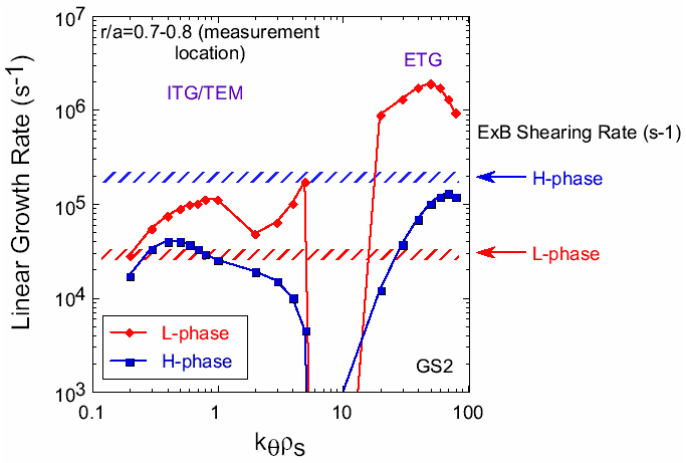

Fig. 9 Linear growth and ExB shearing rates for the L- and H-phases of the discharge whose fluctuation evolution are shown in Fig. 8

growth rates also decrease for all $k_\theta\rho_s$. Furthermore, the linear growth rate in the ITG/TEM range is much less than the ExB shearing rate, consistent with stabilization of this mode and the computed ion transport falling to near neoclassical levels. The linear growth rates in the ETG regime are slightly below the ExB shearing rate, and just how this shearing rate affects the growth of these small-scale ETG modes is a topic that will be addressed through self-consistent non-linear calculations. The inferred χ_e profile shapes for both the L and the H-phases agree with those from an analytic formulation of the electrostatic ETG [16] (for this plasma, β_T at r/a=0.7-0.8 was 1% and 3% for L- and H-mode respectively).

Linear gyrokinetic and non-linear fluid simulations have been used to identify the source of the change in transport levels in the B_T scan. Linear growth rates computed for the discharges in the I_p=0.7 MA, B_T scan are shown in Fig. 10 as a function of $k_\theta\rho_s$ at a radius of r/a=0.65, where the sharp decrease of χ_e with increasing B_T is observed. What is clear from the calculation is the presence of large $k_\theta\rho_s$ modes, indicative of ETG modes, for only the 0.35 T case. Both microtearing and ITG/TEM modes are calculated to be linearly unstable, with comparable growth rates, for all B_T.

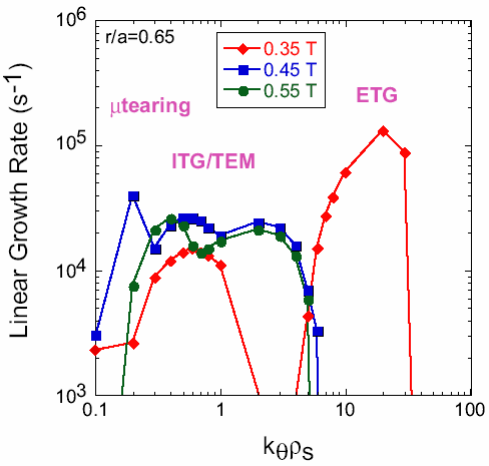

Fig. 10 Linear rates for discharges from the B_T scan at I_p=0.7 MA.

The potential importance of ETG modes in determining the electron transport at B_T=0.35 T has also been indicated by results from a non-linear FLR-modified fluid code [17]. The electrostatic potential in the saturated state is plotted in Fig. 11 for r/a=0.55, and the formation of streamer-like structures with a radial extent of up to 200 ρ_e is clearly seen. The radial streamer structures play a role in enhancing heat transport, and they yield an upper bound for the heat flux by the ETG turbulence. The electron heat flux due to the ETG and these structures approximately is 175 kW/m^2 on average, while the value inferred by TRANSP is between 100 and 130 kW/m^2, consistent with the calculation. Furthermore, the inferred χ_e profile shape at B_T=0.35 T is consistent with that from an analytic formulation of the electromagnetic based ETG [16], while at higher fields, the analytic and experimentally inferred profile shapes do not show good agreement.

5. Conclusions

Experiments on the low aspect ratio, high β_T NSTX have explored the trends and sources of the variations in transport and turbulence across a range of operating conditions. NSTX

confinement shows a strong dependence on toroidal field and a weaker dependence on plasma current, which translates to an $I_p^{1.3-1.5}$ dependence at fixed q, stronger than that in the ITER98PB(y,2) scaling. Dedicated dimensionless parameter scans have shown a strong increase of confinement with decreasing collisionality, and only a very weak degradation with β_T, an important result for success of the advanced operating scenario on ITER. While reduced electron transport resulted in the improvement in confinement with increasing B_T, it is the reduction in ion transport, closely coupled to neoclassical transport levels, that was responsible for the improvement with I_p. Transport characteristics were found to be sensitive to q(r), with the formation of electron ITBs and non-stiff profiles associated with reversed magnetic shear.

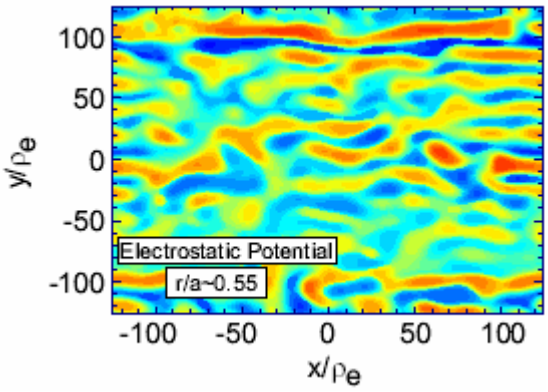

Fig. 11 Non-linear simulation of ETG mode, with the formation for radial streamers at 0.35 T .

Through measurements of turbulence from low to high-k, and through linear and non-linear theoretical calculations, studies to determine the cause of the anomalous electron transport have begun. A decrease in measured turbulence going from L- to H-mode was seen to be associated with a reduction in the inferred electron and ion transport, and the ETG mode was found to be a potential candidate for the electron transport under certain conditions. Future work will focus on assessing the turbulence characteristics as well as more comprehensive non-linear gyrokinetic simulations to identify the source(s) of the anomalous electron transport over a wider range of operating conditions.

A portion of this work was supported in part by U.S. DOE contract DE-AC02-76-CH03073.

References

[1] Kaye, S.M. et al., Nuc. Fusion **45** (2005) S168.
[2] Bell, M. G., et al., Nuc. Fusion **46** (2006) S565.
[3] Smith, D.R. et al., Rev. Sci. Instruments **75** (2004) 38.
[4] Kaye, S. M. et al., Nuc. Fusion **46** (2006) 848**.**
[5] ITER Physics Basis, Nuc. Fusion **39** (1999) 2137.
[6] Cordey, J.G. et al., Nuc. Fusion **45** (2005) 1078.
[7] Kaye, S.M. et al., Plasma Phys. and Controlled Fusion **48** (2006) A429.
[8] Menard, J.E. et al., Phys. Rev. Lett. **97** (2006) 095002.
[9] McDonald, D.C. et al., Plasma Phys. and Controlled Fusion **46** (2004) A215.
[10] Petty, C.C. et al., Phys. Plasmas **11** (2004) 2514.
[11] Kaye, S.M. et al., Nuc. Fusion **24** (1984) 1303.
[12] Houlberg, W.A., et al., Phys. Plasmas **4** (1997) 3230.
[13] Wang, W. et al., Computer Phys. Communications **164** (2004) 178.
[14] Stutman, D. et al., accepted for publication in Phys. Plasmas (2006).
[15] Kotschenreuther, M. et al., Comp. Phys. Comm. **88** (1995) 128.
[16] Horton, W. et al., Phys. Plasmas **11** (2004) 2600.
[17] Horton, W., et al., Nuc. Fusion **45** (2005) 976.